MRS Advances (2023) 8:59–65
https://doi.org/10.1557/s43580-023-00502-8

ORIGINAL PAPER

# Experimental investigation and simulation of Al/$B_4C$ metal matrix composites produced using magnetic field-assisted freeze-casting of porous ceramic structures

Gerardo Gamboa[1] · Zane Wright[1] · Diana Berman[1] · Samir Aouadi[1] · Marcus L. Young[1] · Nicholas Ku[2] · Raymond E. Brennan[2]

Received: 16 September 2022 / Accepted: 10 January 2023 / Published online: 28 February 2023


## Abstract

Magnetic field-assisted freeze-casting was used to create porous $B_4C$ ceramic preforms. An optimum slurry consisted of a mixture of $B_4C$ powders and 6-wt% $Er_2O_3$ powder in a $H_2O$-PVA solution, which was cooled at a rate of 1 °C/min from room temperature to − 30 °C, resulting in porous green state ceramic preforms with vertical channels. Sintered ceramic preforms were then infiltrated in the most vertically aligned channel direction with molten Al (A356) metal through a vacuum-assisted pump to create the metal matrix composite (MMC). The MMCs were imaged using 3D X-ray microscopy and mechanically tested under compression. These results were compared with finite element analysis simulations that verified the anisotropic effect of $B_4C$ channel alignment on mechanical properties. This study highlights magnetic field-assisted freeze-casting as a viable method to create highly directional ceramic preforms, which can be subsequently metal infiltrated to create MMCs.

## Introduction

Anisotropic ceramic preforms for composites have gained attention due to their unique structural possibilities and versatility in applications for high energy damping and impact-resistant materials [1, 2]. Specifically, metal matrix composites (MMCs) show promising characteristics as a physically strong (high impact resistance), yet lightweight and thermally insulating material [3, 4]. Furthermore, MMCs can be fabricated through cost-effective methods, such as a two-step process of magnetic field-assisted freeze-casting followed by metal infiltration [5]. Traditional freeze-casting has been shown to create porous preforms with channels aligned in the direction of ice solidification under dynamic cooling conditions [6]. However, these channels lack precise control, and channels in the direction perpendicular to freezing lack any alignment [7].

Therefore, the goal of this study was to create anisotropic A356 Al/$B_4C$ MMCs by magnetic field-assisted freeze-casting of a ceramic $B_4C$ preform followed by vacuum-assisted metal infiltration with an A356 Al alloy. Magnetic nanoparticles have been shown to align themselves in the direction of the magnetic field in previous studies when magnets are placed around the solidifying slurry [7]. In this study the effect of magnetic erbium oxide ($Er_2O_3$) nanoparticles is observed and used due to its potential found in our previous work [8]. This resulted in a composite with directionally controlled mechanical properties, which was predicted by rule-of-mixtures (ROM) and finite element analysis (FEA) models.

Predictions from the ROM models can be made about the Young's modulus of the A356 Al/$B_4C$ MMC, where the properties are expected to be closer to the lower bound material (A356 Al) in the weak direction and closer to the upper bound material ($B_4C$) in the strong direction. In Young et al. [9], modifications to the ROM models were made from Eqs. 1 and 2, which has two phases for the ceramic constituent part (each phase having its own volume fraction *f1*, *f2*, and *f3*) and the Young's modulus defined for the metal and ceramic as $E_{met}$ and $E_{cer}$, respectively [9].

$$E_{c,\text{longitudial}} = f_1 E_{\text{met}} + (f_2 + f_3) E_{\text{cer}}, \quad (1)$$

✉ Marcus L. Young
Marcus.Young@unt.edu

1 Department of Material Science and Engineering, University of North Texas, Denton, TX, USA

2 DEVCOM Army Research Laboratory, Aberdeen Proving Ground, Aberdeen, MD, USA

$$E_{c,\text{transverse}} = \left(\frac{f_1 E_{\text{met}}}{-\nu_{\text{met}}} + \frac{(f_2 + f_3)E_{\text{cer}}}{-\nu_{\text{cer}}}\right). \quad (2)$$

FEA models can help provide a visual image of the stress distribution and overall stress of the MMC. An Al/$B_4C$ MMC created by magnetic field-assisted freeze-casting and followed by vacuum-assisted metal infiltration, which exhibits its shared properties of the alloy and ceramic that are tunable for the desired application, is presented and compared with the ROM and FEA predictions.

## Materials and methods

$B_4C$ powder (US Research Nanomaterials, Inc., Houston, TX, USA) with 99.9% purity (1–3-µm particle size) was used as the base ceramic for the slurry, mixed with 6-wt% $Er_2O_3$ (American Elements, Los Angeles, California, USA) with 99% purity (less than 100 nm in particle size) and deionized (DI) $H_2O$ as a solvent with 5-wt% polyvinyl alcohol (PVA). The PVA was pre-mixed in the DI $H_2O$ at 90 °C to help spread the binder evenly when mixed with the ceramic slurry [7]. Next, the $B_4C$ and $Er_2O_3$ powders were added and continually mixed until a visible increase in the viscosity was observed (Fig. 1 (top)).

A magnetic field-assisted method was used in combination with a four-step cooling rate to create the porous $B_4C$ preform [10]. A copper plate with an attached thermocouple was wrapped around the top of the plate, placed above an insulating box containing liquid nitrogen, and cooled to 0 °C from room temperature. Next, the prepared slurry was poured into a 25.4-mm diameter high-density polyethylene (HDPE) cylindrical mold sandwiched between two sets of three neodymium disc magnets (32 mm in diameter, thickness of 3.175 mm, separated 15 mm apart resulting in an overall magnetic field with a strength of 1.44 Tesla (Kg/As$^2$) in the center of the slurry using equations from our related work) [7], where the whole setup including the slurry, mold, and magnets were placed on top of the copper plate and remained above the liquid nitrogen box (Fig. 1 (top)) during the cooling step. Additional liquid nitrogen was added by a funnel until the plate was cooled to − 30 °C at a rate of − 1 °C/min. The solid frozen slurry was then sublimated as described in Bakkar et al. [7]. After sublimation, the $B_4C$ green body was sintered in a vacuum furnace from room temperature

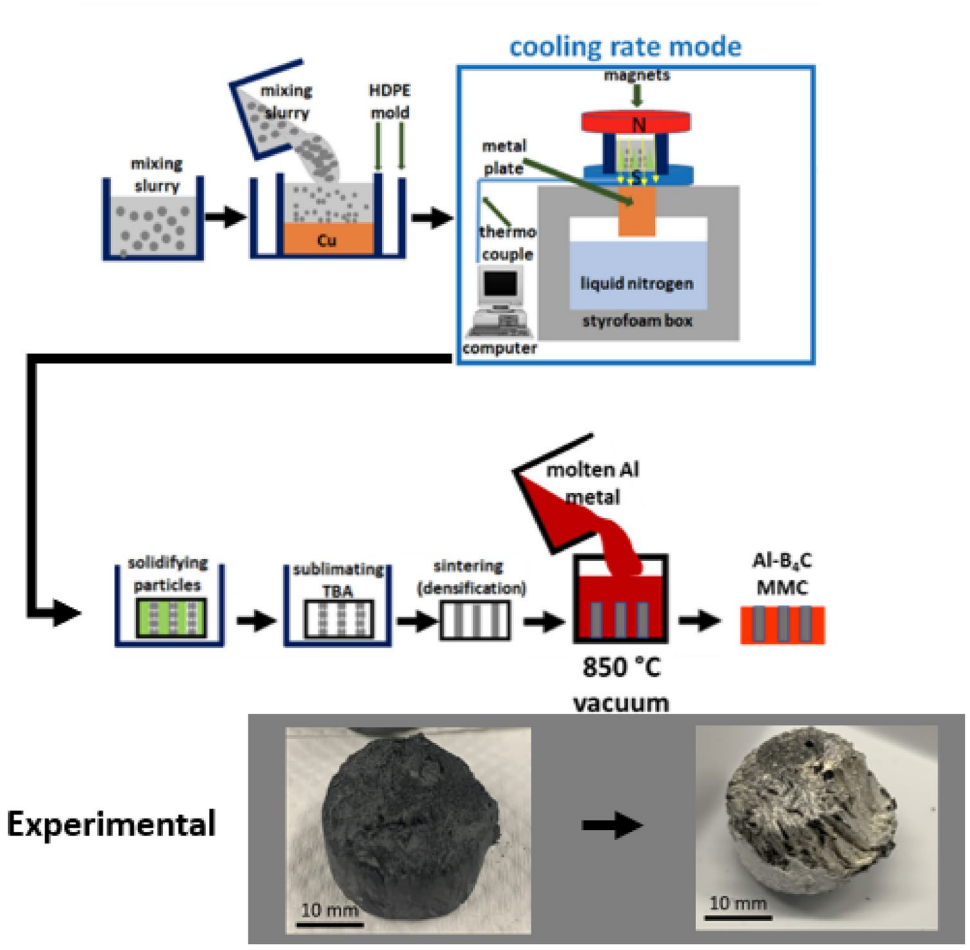


**Fig. 1** Schematic illustrating the magnetic field-assisted freeze-casting method and subsequent metal infiltration method for creating Al/$B_4C$ MMCs. The mold is filled with a ceramic slurry which is then continuously cooled to create green $B_4C$ preforms, which are then sublimated and sintered for subsequent metal infiltration using A356 Al alloy. After sintering is complete, the $B_4C$ preform is metal infiltrated with A356 Al alloy, thus creating an Al/$B_4C$ MMC. Examples of the sintered ceramic and infiltrated $B_4C$ ceramic with A356 Al alloy are also shown

up to 600 °C, held at 600 °C for 2 h to burn out the PVA, then heated up to 2000 °C, held for two hours to sinter the ceramic particles, and then cooled down to room temperature at a rate of 5 °C/min (Fig. 1 (middle)).

The sintered $B_4C$ preform was infiltrated with a molten A356 Al alloy. To prepare the $B_4C$ for infiltration, the sample was placed in a cylindrical ceramic tube to hold a wax mold with openings on the top and bottom of the mold to guide the molten aluminum. The wax mold and Al alloy in the graphite crucible were placed into a furnace and heated up to 850 °C for 15 min to ensure the Al alloy was completely molten before being placed into the guide with vacuum-assisted infiltration through the bottom opening. The resultant Al/$B_4C$ MMC, which was approximately 25 mm in diameter and 18 mm in height (Fig. 1 (bottom)), was ready for characterization. It was also cut into compression samples with a diamond wire saw in 1:1:2.1 ratio resulting in approximately $5 \times 5 \times 10.5$ mm samples.

Sintered ceramic preforms, infiltrated samples, and compression samples cut from infiltrated preforms were 3D imaged in air on a rotating stage using a Zeiss Xradia 520 Versa X-ray microscopy (XRM) machine at a $0.4 \times$ optical magnification on the objective mirror with an average exposure time of 2.5 s. Tomographic reconstructions of the model were generated using Dragonfly software [11] to recreate the slices into a 3D model from which physical properties such as porosity percentage, channel size, and elemental distribution of the sample were determined.

## Simulations

Simulation models were created in Abaqus FEA to predict the behavior of composite samples under compression. A cube model with alternating "layers" of ceramic and alloy was used to approximate the sample geometry for simplicity. The dimensions of the simulation were comparable to the data obtained from the experimental XRM ceramic. The model ceramic was then defined as only elastic, while the alloy was defined as elastic and plastic, with values from literature [12, 13]. Boundary conditions were applied on opposite faces, with one fixed and the other evenly loaded to deform by up to 10%. A mesh of 67,200 units was created. The model was simulated to analyze the mechanical response obtained by stress–strain curves from the reaction force and percent compression. Several models of increasing size were created to find the minimum acceptable size for compression testing modeling. A model size of 200 $\mu m^3$ with two channels was found to be acceptable and used for extensive compression testing in the aligned and perpendicular directions to infiltration, as shown in Fig. 2a. Additionally, a cube model from the XRM reconstruction was created to investigate the effect of real geometry and imperfections on the sample behavior (Fig. 2d) and compressed in a similar manner to the simulated cube referenced above.

## Testing

Compression samples were made from the infiltrated MMC, porous $B_4C$, and bulk A356 Al alloy in a ratio of approximately 1:1:2.1. A bulk sample of the Al alloy was used

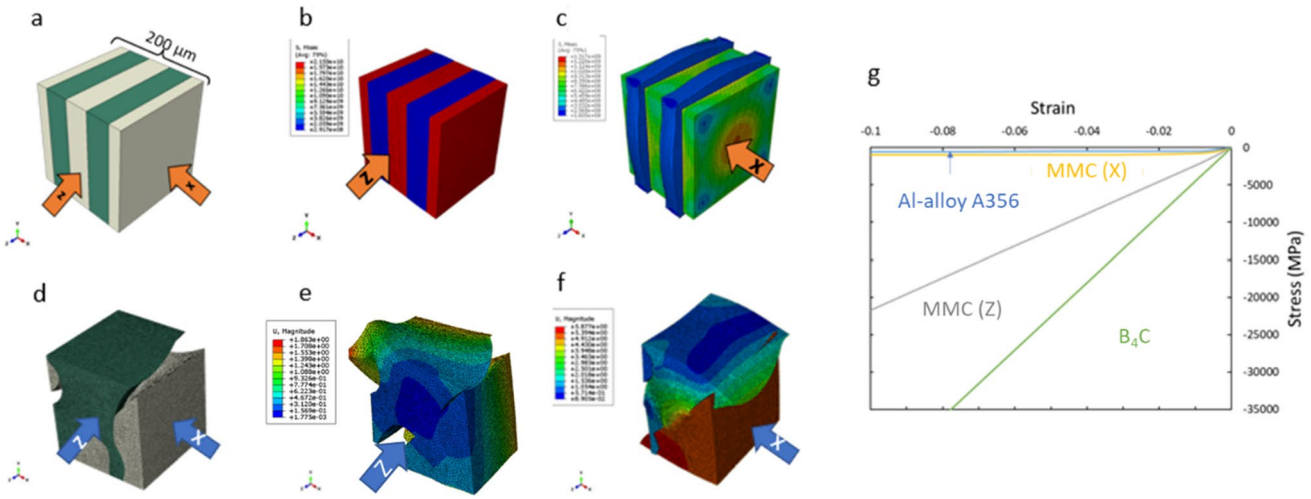


**Fig. 2** Abaqus FEA model of the simulated 200-µm cube (**a**) with 50/50 A356 Al alloy (green)/$B_4C$ (gray) showing the stress in the z- (**b**) and x-directions (**c**) labeled with the orange arrows. An Abaqus FEA model of real-sample geometry imported from the XRM reconstruction and **d** cut to a 200-µm cube to match the simulated cube geometry with compression in the (**e**) z-direction (**f**) and x-direction. **g** Simulated stress–strain curves for the 50/50 MMC compared to pure bulk materials of A356 Al alloy and $B_4C$. XRM model stress–strain plots could not be created due to the complex geometry limiting the model to the elastic deformation portion

to set a baseline for the expected minimum and maximum values of the composite. All samples were compressed on a Shimadzu AGS-X loading frame equipped with a 10-kN load cell at a constant rate of 0.005 in/in/min per ASTM standard [14].

## Results

The XRM reconstruction determined that the average channel size for the sintered ceramic sample was about 50 µm across before infiltration, which was consistent with previous results [5]. Due to its higher density, the Al alloy was highlighted as bright streaks along the solidification front at approximately a 20-degree angle to the z-direction (Fig. 3b). This orientation resulted in some channels not being filled during metal infiltration, leading to porosity in the final MMC (Fig. 3c–d). Al alloy infiltration did not always fill single channels, but instead broke parts of the ceramic preform while taking the path of least resistance and leaving some porosity behind. The Al alloy channels varied in size from around 50 to 620 µm and were oriented along the solidification direction. Due to the variety of distribution in the final infiltrated MMC, compression samples cut from the full sample were scanned again, with the composition of each sample recorded before compression. A representative MMC shown in Fig. 3e with a composition of 58.3-vol% $B_4C/ErO_2$, 21.6-vol% A356 Al alloy, and 20.1-vol% porosity (air). These compositional values were obtained using the Dragonfly region of interest (ROI) tool (Fig. 3f).

The simulated 200-µm cube with 50% A356 Al alloy infiltration, in the z-direction (parallel with infiltration and identical to the y-direction for all simulations) showed mostly elastic behavior with an estimated Young's modulus of 247.9 GPa (Fig. 2b). This value was within the expected range, falling between the bulk $B_4C$ and A356 Al alloy simulations (i.e., 450 and 70 GPa, respectively), as shown in Table 1 and Fig. 2g. During compression in the z-direction, as shown in Fig. 2b, the Al alloy regions were constrained by the adjacent $B_4C$ walls. Thus, the model compression shows mostly linear elastic deformation of both the ceramic and metal, with a small amount of plastic deformation in the metal. During compression in the x-direction (perpendicular to infiltration) as shown in Fig. 2c, the Al alloy regions were unconstrained, since they were sandwiched between the $B_4C$ plates. Therefore, the model compression shows mostly elastic–plastic deformation of the metal and some elastic deformation in the ceramic. In this case, the estimated Young's modulus dropped to 139.7 GPa, with plastic deformation occurring at less than 1% strain. These values match well

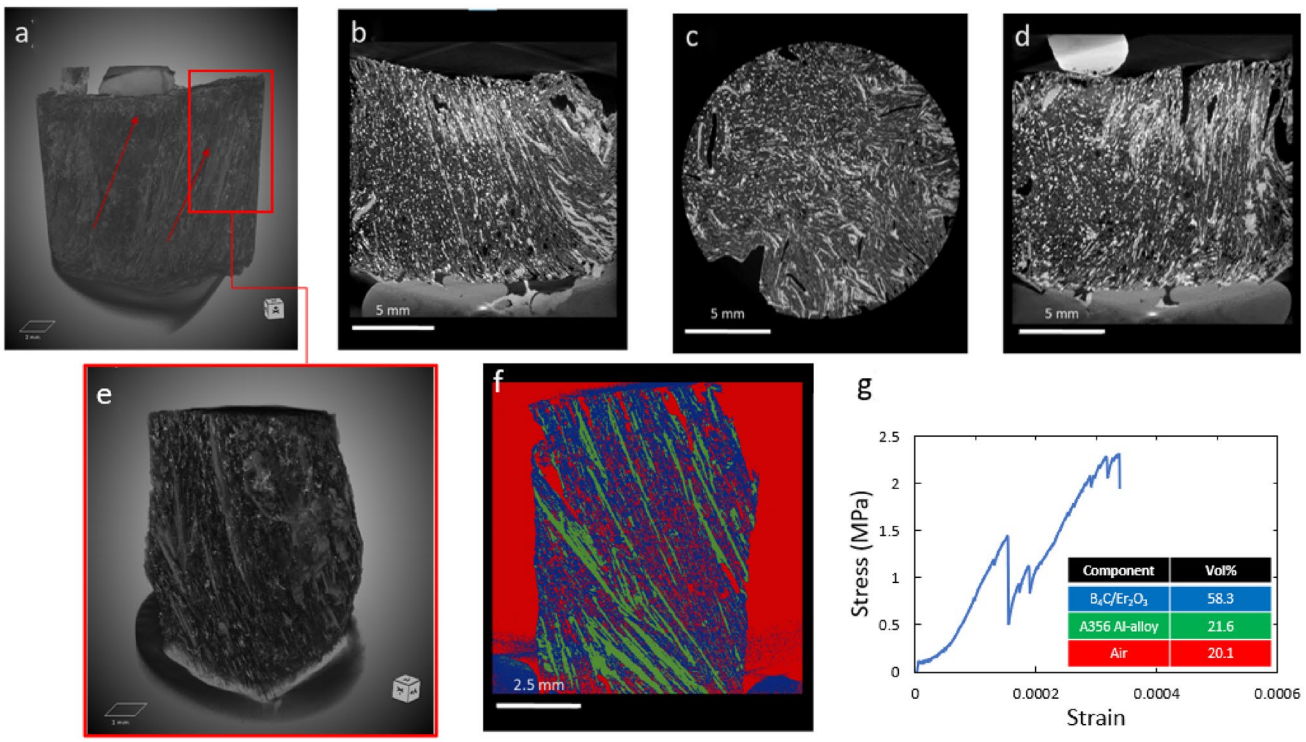


**Fig. 3** **a** XRM reconstruction of the final infiltrated Al/$B_4C$ MMC sample shown with **b** xz, **c** xy, and **d** yz projections. **e** A compression sample cut from the full MMC is shown with the **f** xz projection to highlight different components tabulated by volume % with the **g** resultant stress–strain curve with fracture events seen as sharp drops in the curve seen at less than 0.0002 and 0.0004 strain

**Table 1** Young's Modulus values using rule-of-mixtures models (ROM-Z and ROM-X), FEA simulations for 50-vol% A356 and 50-vol% B4C (50%-Z and 50%-X), FEA simulations from XRM models (XRM-Z and XRM-X), literature values (A356 Al alloy and $B_4C$), and experimentally determined Al-$B_4C$ MMC sample

| Sample | Young's Modulus (GPa) |
|---|---|
| ROM-Z | 260 |
| ROM-X | 121 |
| 50%-Z | 248 |
| 50%-X | 140 |
| XRM-Z | 201 |
| XRM-X | 124 |
| A356 Al Alloy | 70 |
| $B_4C$ | 450 |
| Al-$B_4C$ MMC | 10 |

with the ROM models for composites with fibers, as shown in Table 1, with the upper bound related to the z-direction and the lower bound related to the x-direction. The model extracted from the XRM was shaped to be the same size as the simulated cubes, included porosity with an overall composition of approximately 55-vol% $B_4C$, 34-vol% A356 Al alloy, and 11-vol% porosity, as shown in Fig. 2d.

Compression testing was performed on three Al/$B_4C$ MMC samples in the z-direction, in addition to a sample of bulk A356 Al alloy. The compression results were therefore adjusted by a strain factor using bulk A356 Al alloy as a calibrant. MMC samples showed composite behavior with staggered peaks of increasing stress followed by sharp drops due to fracture events occurring in the composite. This was associated with fracturing of individual channels and struts (Fig. 2g). The Young's modulus of all samples was determined from the linear portion of the stress–strain curve before a major fracture event.

## Discussion

Magnetic field-assisted freeze-casting proved successful in creating a ceramic body with aligned channels for infiltration, as observed in Fig. 3b. These results are in good agreement with previous use of a magnetic field to align the ceramic slurry channels [5]. A slow cooling rate resulted in larger channels (30 to 100 µm), comparable to the channels widths made in this study ($50 \pm 8$ µm) before infiltration. These channels are still seen most clear at the bottom of the full composite of Fig. 3b where the composite was least impacted by the A356 solidification.

A356 Al alloy was easily identified in the XRM imaging ROI tool in Fig. 3b–d as the brighter-colored phase due to its higher density as compared to the $B_4C$ preform. However, due to the unconventional experimental setup as compared to other infiltration systems during the short transition period from moving the molten A356 Al alloy into the sample, the Al alloy cooled rapidly becoming more viscous, making it more difficult to completely infiltrate the $B_4C$. Ultimately, the resultant MMC was a four-phase composite with approximately 58-vol% $B_4C/Er_2O_3$, 22-vol% A356 Al alloy, and 20-vol% porosity. Large pores were formed mostly at the bottom of the sample due to the A356 unable to flow easily. The rotated orientation of the channels seen clearest in Fig. 3b made infiltration of the composite more difficult leading to some pores in the size and shape of the non-infiltrated ceramic. Also, due to the weak strength of the ceramic, several large pores, a couple hundred micrometers in size, are formed at the top of the sample as weaker walls collapse and create pockets of air.

For simplicity, all FEA simulations assumed a fully infiltrated Al/$B_4C$ MMC with no perpendicular struts in the structure. When compressed in the z-direction, the composite was observed to have a higher Young's modulus and yield stress due to being under iso-strain conditions compared to the iso-stress conditions in the x-direction. This can be observed clearly in Fig. 2b, where the $B_4C$ and A356 Al alloy phases in the z-direction were compressed evenly, and the defined boundary conditions and $B_4C$ walls held the composite together. In contrast, the lack of supporting layers or boundary conditions adjacent to the plastic A356 Al alloy regions in the x-direction allowed free movement under much lower loads. Therefore, the simulated MMC displayed highly anisotropic behavior, as expected, with more ceramic-like behavior in the z-direction and more metallic-like behavior in the x-direction.

The model created from the XRM scan showed a more realistic response and captured some of the effects of the scaffold geometry made during freeze-casting, and the air from incomplete infiltration. As observed in Fig. 2d–f, the porosity of incompletely filled channels led to weaker zones and sudden movement in both the z- and x-directions. However, the "bridge" geometry of the $B_4C$ provided support areas, not present in the theoretical models (Fig. 2a). These cross-supports or struts kept the Young's modulus relatively high despite the porosity.

The experimental results from compression testing MMC samples did not match well with finite element simulations. However, experimental results from compression testing of A356 Al alloy exhibited values that matched very closely with those from the FEA simulations and from literature (Young's modulus of 70 GPa and yield stress of approximately 250 MPa), indicating good values were used for the Al alloy in the simulation and validating the compression testing methodology. The highest value of Young's modulus for the experimental MMC samples was 10 GPa, as shown in Table 1. The extremely low strength was likely due to the arrangement of porosity within the relatively large shape of the sample compared to the simulation (10 mm vs. 200 µm). In the XRM-obtained simulated model, the porosity, while

still a high-volume percent, was not aligned and was contained to a localized area due to the small model size. However, large, aligned porous regions of only $B_4C$ and pores in the experimental composite samples are observed in Fig. 3f. These continuous columnar regions of porosity had a large impact on the cross-sectional area calculations and fracture mechanics of the sample. This is most evident by the sharp curve drops in Fig. 3g indicative of a fracture event where the composite collapses suddenly until a more solid cross-section is reached. For the calculations, the cross-sectional area of the solid sample was much lower than what was calculated based on geometry. Thus, the actual stress was also much higher when calculated by Hooke's Law, where the force is equal to the stress divided by the cross-sectional area. It is recommended to improve the mechanical strength and fracture toughness of the Al/$B_4C$ MMC that the metal infiltration align with the direction of the columnar growth, thus ensuring a low viscosity metal can flow continuously through sample to avoid early fracture of the columns during infiltration and reduce or eliminate porosity in the sample.

## Conclusion

The experimental Al/$B_4C$ MMC showed the vital importance of all processing steps in magnetic field-assisted freeze-casting and metal infiltration of the composite. Depending on the cooling rate of the ceramic preform, the channel size increased with slower cooling rates, thus creating larger channels. Complete infiltration of the channels was vital to avoid residual porosity in the sample. Larger channels inherently led to better infiltration, but also lowered the mechanical strength and fracture toughness. Regardless of channel size, infiltration was still limited when the low viscosity melt of A356 Al alloy could not be reached. Considering the weak ceramic structure, the alloy should be allowed to infiltrate the $B_4C$ as liquid to prevent creating a large difference in channel size and trapped porosity. If infiltrated this way, room-temperature cooling would be sufficient. These processing variables made obtaining composite samples that matched the ideal conditions set in the simulation difficult to achieve. The structures before and after infiltration were characterized using XRM imaging, highlighting some of the effects of processing variables, such as off-axis channel alignment and excess porosity. The final Al/$B_4C$ MMC samples were found to have been partially infiltrated with A356 Al alloy along, with large, aligned areas of porosity leading to early failure during compression testing, falling short of theoretical simulated ROM, and FEA model properties.

**Acknowledgments** The authors would like to thank Dr. Said Bakkar for useful discussions and insights into experimental procedures. The authors would like to thank Dr. Sheldon Shi and Mr. Lee Smith for assistance with mechanical (compression) testing. The authors would like to thank Johnathan Rodriguez and Evan Ober for their assistance with X-ray microscopy. This work was performed, in part, at the University of North Texas's (UNT) Materials Research Facility (MRF) and at UNT's Advanced Materials and Manufacturing Processes Institute (AMMPI). This research was supported by DEVCOM Army Research Laboratory (Award No. W911NF-19-2-0011).

## Declarations

**Conflict of interest** The authors have no conflict of interest to declare at this time.

## References

1. M.A. Ghadkolai, S. Creager, J. Nanda, R.K. Bordia, Freeze tape cast thick Mo Doped $Li_4Ti_5O_{12}$ electrodes for lithium-ion batteries. J. Electrochem. Soc. **164**(12), A2603–A2610 (2017). https://doi.org/10.1149/2.1311712jes
2. M.-A. Shahbazi, M. Ghalkhani, H. Maleki, Directional freeze-casting: a bioinspired method to assemble multifunctional aligned porous structures for advanced applications. Adv. Eng. Mater. **22**(7), 2000033 (2020). https://doi.org/10.1002/adem.202000033
3. P. Niksiar, M.B. Frank, J. McKittrick, M.M. Porter, Microstructural evolution of paramagnetic materials by magnetic freeze casting. J. Market. Res. **8**(2), 2247–2254 (2019). https://doi.org/10.1016/j.jmrt.2018.12.024
4. S. Deville, E. Saiz, R.K. Nalla, A.P. Tomsia, Freezing as a path to build complex composites. Science (1979) **311**(5760), 515–518 (2006). https://doi.org/10.1126/science.1120937
5. S. Bakkar et al., Al/$Al_2O_3$ metal matrix composites produced using magnetic field-assisted freeze-casting of porous ceramic structures. J. Mater. Res. **36**(10), 2094–2106 (2021). https://doi.org/10.1557/s43578-021-00159-9
6. G. Shao, D.A.H. Hanaor, X. Shen, A. Gurlo, Freeze casting: from low-dimensional building blocks to aligned porous structures: a review of novel materials, methods, and applications. Adv. Mater. **32**(17), 1907176 (2020). https://doi.org/10.1002/adma.201907176
7. S. Bakkar et al., Controlling anisotropy of porous $B_4C$ structures through magnetic field-assisted freeze-casting. Ceram. Int. **48**(5), 6750–6757 (2022). https://doi.org/10.1016/j.ceramint.2021.11.226
8. C. Moorehead, V. Blair, N. Ku, R. Brennan, The effect of rare-earth dopants on the texturing of alumina under high-strength magnetic field. Mater. Chem. Phys. **241**, 122388 (2020). https://doi.org/10.1016/j.matchemphys.2019.122388
9. M.L. Young, R. Rao, J.D. Almer, D.R. Haeffner, J.A. Lewis, D.C. Dunand, Load partitioning in $Al_2O_3$–Al composites with three-dimensional periodic architecture. Acta Mater. **57**(8), 2362–2375 (2009). https://doi.org/10.1016/j.actamat.2009.01.019
10. S. Bakkar et al., Design of porous aluminum oxide ceramics using magnetic field-assisted freeze-casting. J. Mater. Res. **35**(21), 2859–2869 (2020). https://doi.org/10.1557/jmr.2020.197
11. Dragonfly. Object Research Systems
12. R. Peter, *Metals Handbook - Properties and Selections: Nonferrous Alloys and Special-Purpose Materials*, 10th edn. (ASM International, Materials Park, 1990)

13. H.O. Pierson, *Handbook of Refractory Carbides and Nitrides: Properties, Characteristics, Processing and Applications* (Noyes, Norwich, 1996)
14. ASTM International, *ASTM E9–09*, vol. 3 (ASM International, Materials Park, 2018)